Quantum carpets in a leaky box: Poincaré's recurrences in the continuous spectrum

M. Ćosić ●[*]

Laboratory of Physics, Vinča Institute of Nuclear Sciences - National Institute of the Republic of Serbia,
University of Belgrade, P.O. Box 522, 11001 Belgrade, Serbia

The freedom to define branch cuts of the complex function is used to derive an integral representation of the quantum carpet, thus producing a generalization of the Poincaré recurrence theorem in the case of the continuous spectrum. This approach provides a different way to renormalize resonant states to be both space and time convergent. The coherence of quantum carpets was related to the properties of the Wigner function in the canonical time-frequency phase space. It has been shown that the distortion of the Wigner function shape is directly responsible for the lack of the ability of the dynamics to produce revivals equally as sharp as the initial wave packet.

I. INTRODUCTION

A quantum carpet is a pattern—generated by a wave propagating in a dispersive medium—characterized by regular spontaneous reconstructions of the original wave packet and its copies [1]. Carpets were observed in optics [2,3], Bose-Einstein condensates [4], cold-atom waves [5,6], and multimode waveguides [7], to name just a few. In all these examples, carpets were formed by a discreet superposition of waves whose phases are a quadratic function of the summing index, and their properties were determined by Gauss sums of the number theory [8,9]. Soon it was realized that the carpet is a pattern associated with the first in the hierarchy of the revival effects related to the cubic, quartic, etc., phase functions [10]. Thus, carpets are quantum manifestations of the Poincaré recurrence theorem, stating that a volume-preserving discrete state-space system must revisit its initial state infinitely often [11].

The purpose of this paper is to show that continuous superpositions can produce carpets. In that regard, we will analyze the evolution of a quantum particle in a leaky-box potential

$$V(q) = V_o[\delta(q - a) + \delta(q + a)], \tag{1}$$

where $2a$ is the length of the box, while parameter $V_o > 0$ controls the amplitude of the tunneling current. At first glance, the substitution of eigenstates by resonances [12,13] provides the desired generalization. This approach is inadequate for several reasons. Outgoing time-decreasing resonances are spatially divergent, implying the existence of the self-amplification mechanism operating in the free space. Resonances are not complete, nor orthogonal. Interpreting complex eigenvalues of an arbitrary operator or making sense of complex probability densities is far from trivial. Addressing these issues

sparked the development of the theory of rigged Hilbert spaces [14].

It will be shown how to utilize the freedom to define the branch cut and sheets of the complex function to obtain physically acceptable resonant states without the mentioned artifacts. The proposed model applies to imperfect waveguides, where part of the wave can escape the resonator, or to real dynamics of trapped atoms where an external field is used to suppress tunneling and obtain the quadratic phase function [4].

Understanding the coherence-loss process is important in itself since there are many proposals for applications of carpets in metrology [15], number-theoretic computing [16–18], quantum information processing [19], or as a tool for studying interactions between ultracold fermions [20]. The coherence of the obtained carpets will be the subject of a separate analysis, which will focus on the spectral properties of the nondecay probability. It will be shown that synchronization between spectrogram modes is responsible for the creation of extrema of the nondecay probability function, while their deformation is responsible for the creation of the wider extrema of the reduced amplitude. A similar approach was used to explain the quantum rainbow effect by the coordinated self-interference of wave packets [21–23].

There are proposals to use the distortion of quantum carpets to study decoherence processes [24–26]. The presented model can also be used for that purpose. It will be shown that tunneling leads to the suppression of interference between resonant states, thus inducing decoherence. However, tunneling alone is not capable of producing complete decoherence. Nevertheless, the presented simple, solvable model shares many features of the effective decoherence models [24–26], or more elaborate numerical investigations [27–29]. An additional advantage is that all physical quantities, such as the energies and lifetimes of resonant states that are are functions of V_o, have a clear physical interpretation. The derived model has effectively only one free parameter controlling the strength of decoherence, instead of the abstract parameter used in Refs. [24–26].

---

[*]Corresponding author: mcosic@vinca.rs

042218-1

II. DYNAMICS OF QUANTUM CARPETS

A. The integral representation

The time development of the initial state ψ_0 is given by

$$\psi(q,t) = \int_{-\infty}^{\infty} K(q,\bar{q},t)\psi_0(\bar{q})d\bar{q}, \qquad (2)$$

where K is the propagator. Its associated Green's function is defined by Fourier's transform of the propagator and is a function of the real energy E. An analysis of resonances requires an analytical continuation of the Green's function to the whole complex plane. Therefore, it will be defined by Laplace's transform

$$G(q,\bar{q},\lambda) = \int_{-\infty}^{\infty} K(q,\bar{q},t)\exp[-\lambda t]dt. \qquad (3)$$

For potential (1), the Green's function is given by the expression [30]

$$G(q,\bar{q},\lambda) = \frac{\begin{bmatrix} G_{\mathrm{f}}(q,\bar{q}), & G_{\mathrm{f}}(q,-a), & G_{\mathrm{f}}(q,a) \\ G_{\mathrm{f}}(-a,\bar{q}), & G_{\mathrm{f}}(-a,-a)+\frac{1}{V_o}, & G_{\mathrm{f}}(-a,a) \\ G_{\mathrm{f}}(a,\bar{q}), & G_{\mathrm{f}}(a,-a), & G_{\mathrm{f}}(a,a)+\frac{1}{V_o} \end{bmatrix}}{\begin{bmatrix} G_{\mathrm{f}}(-a,-a)+\frac{1}{V_o}, & G_{\mathrm{f}}(-a,a) \\ G_{\mathrm{f}}(a,-a), & G_{\mathrm{f}}(a,a)+\frac{1}{V_o} \end{bmatrix}}, \qquad (4)$$

where

$$G_{\mathrm{f}}(q,\bar{q},\lambda) = \frac{1}{\sqrt{-i\lambda}}\exp[-2\sqrt{-i\lambda}|q-\bar{q}|] \qquad (5)$$

is the free-space Green's function expressed in units where $a = 1/2$, $\hbar = 1$, and $m = 2$, which is convergent for $\mathrm{Re}\{\lambda\} > 0$ [31]. A λ representation of the wave function is defined by the integral

$$\Psi(q,\lambda) = \int_{-\infty}^{\infty} G(q,\bar{q},\lambda)\psi_0(\bar{q})d\bar{q}. \qquad (6)$$

It is assumed that $\psi_0 = \delta(x)$. This choice simplifies the analysis considerably but does not affect the generality of its conclusions. Outside the box ($|q| > 1/2$), the λ representation of the wave function reads

$$\Psi(q,\lambda) = \frac{\exp[-2\sqrt{-i\lambda}|q|]}{V_o + \sqrt{-i\lambda} + V_o\exp[-2\sqrt{-i\lambda}]}, \qquad (7)$$

while inside the box ($|q| \leqslant 1/2$) it is given by the expression

$$\Psi(q,\lambda) = \frac{1}{\sqrt{-i\lambda}}\exp[-2\sqrt{-i\lambda}|q|]$$
$$\times \frac{2V_o\exp[-2\sqrt{-i\lambda}]\cosh[2\sqrt{-i\lambda}|q|]}{\sqrt{-i\lambda}(V_o + \sqrt{-i\lambda} + V_o\exp[-2\sqrt{-i\lambda}])}. \qquad (8)$$

Due to the factor $\sqrt{-i\lambda}$, functions (7) and (8) have a branch point at $\lambda = 0$, a branch cut along the negative $\mathrm{Im}\{\lambda\}$ axis, and are both double valued. The principal branch $\Psi_1(q,\lambda)$ is obtained for $\arg\{\lambda\} \in [-\pi,\pi)$, while the secondary branch $\Psi_2(q,\lambda)$ is obtained for $\arg\{\lambda\} \in [\pi,3\pi)$. Passing onto the second sheet, the factor $\sqrt{-i\lambda}$ transforms into $-\sqrt{-i\lambda}$.

The morphology of these functions can be very different as demonstrated in Figs. 1(a) and 1(b) showing the $q = 0$ slice through the complex functions Ψ_1 and Ψ_2. The secondary sheet contains symmetrical pairs of poles $\lambda_{2n}^{(p)} = i\eta_{2k}^2$ and $\lambda_{2k+1}^{(p)} = i\eta_{2k+1}^2$ ($k = 1, 2, \ldots$), that are solutions of the equation $V_o - \eta + V_o\exp[2\eta] = 0$, ($\eta = -\sqrt{-i\lambda}$, thus $\mathrm{Re}\{\eta_n\} > 0$, for $n = 1, 2, \ldots$). On the contrary, the principal sheet has no poles but ordinary maxima $\lambda_n^{(\mu)}$ at $\approx i\,\mathrm{Im}\{\lambda_{2n}^{(p)}\} = i\,\mathrm{Im}\{\lambda_{2n+1}^{(p)}\}$.

The evolution of the wave function is now given by the inverse Laplace's transform of $\Psi(q,\lambda)$. For its evaluation, it is advantageous to introduce the coordinate transformation $\bar{\lambda} = -i\lambda$, that aligns the $\mathrm{Re}\{\bar{\lambda}\}$ axis with the $\mathrm{Im}\{\lambda\}$ axis. Thus, $\psi(q,t)$ is given by the following contour integral,

$$\psi(q,t) = \frac{1}{2\pi}\int_B \Psi(q,\lambda = i\bar{\lambda})\exp[i\bar{\lambda}t]d\bar{\lambda}, \qquad (9)$$

where all singularities of the integrand should be on the left of Bromwich's integration contour B. Regardless of the
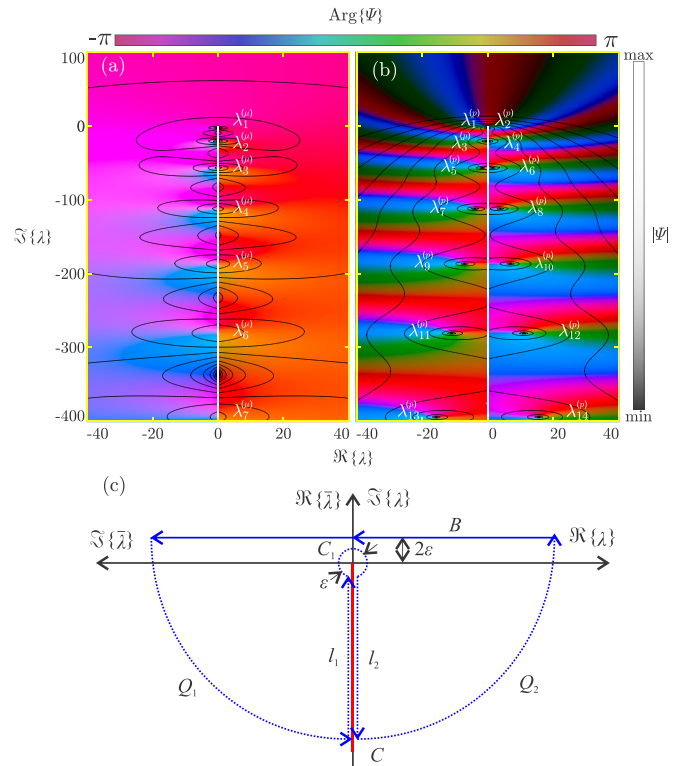

FIG. 1. The domain color representation of (a) $\Psi_1(q=0,\lambda)$ and (b) $\Psi_2(q=0,\lambda)$. The black lines show the contours of its modulus, while white lines show the branch cuts. (c) Optimal contour for evaluation of the inverse Laplace's transform.

sheet used, the optimal integration contour is parallel to the $\mathrm{Re}\{\bar{\lambda}\}$ axis displaced by a small distance 2ε. Its complement—consisting of quarter circles Q_1 and Q_2 of large radius R, a circle C_1 of radius ε around the branch point, and lines l_1 and l_2 displaced by $\varepsilon/2$ to the left and right from the branch cut—is shown in Fig. 1(c). Together they form the closed contour enabling the evaluation of integral (9) by contour integration. In the limit $\varepsilon \to 0$ and $R \to \infty$, the contribution of segments Q_1, Q_2, and C_1 becomes negligible, reducing integral (9) to the sum $\psi(q,t) = \psi_B(q,t) + \psi_R(q,t)$. Here, ψ_B represents the contribution of the branch cut,

$$\psi_B(q,t) = \frac{e^{i\pi}}{2\pi} \int_\infty^0 \Psi(q; \bar{\lambda} = \zeta e^{i\pi}) \exp[i\zeta e^{i\pi}t]d\zeta \tag{10}$$
$$+ \frac{e^{-i\pi}}{2\pi} \int_0^\infty \Psi(q; \bar{\lambda} = \zeta e^{-i\pi}) \exp[i\zeta e^{-i\pi}t]d\zeta,$$

while ψ_R stands for the sum of resonances,

$$\psi_R(q,t) = \sum_n i \operatorname*{Res}_{\bar{\lambda}=\eta_n^2}\{\Psi\} \exp\left[i\eta_n^2 t\right], \tag{11}$$

associated with residues enclosed by the contour.

The convergence of integral (9) determines the optimal integration contour but says nothing about which sheet of Ψ to use. The standard approach mandates the use of Ψ_2 [13] since at first glance only this choice for $V_o \to \infty$ produces the carpet for the sealed box [8]. As usual, this choice leads to finite ψ_B for $|q| \gg 1/2$,

$$\psi_B(q,t) = \int_0^\infty \mathrm{Im}\left\{\frac{\exp[-2i\sqrt{\zeta}|q|]}{V_o + i\sqrt{\zeta} + V_o \exp[-2i\sqrt{\zeta}]}\right\}$$
$$\times \exp[-i\zeta t]\frac{d\zeta}{i\pi}, \tag{12}$$

and a diverging contribution of resonances

$$\frac{\eta_n}{V_o - \eta_n + \frac{1}{2}} \exp\left[2\eta_n|q| + i\eta_n^2 t\right], \tag{13}$$

because $\mathrm{Re}\{\eta_n\} > 0$, for all n.

Note that this is not the only choice. When the first sheet is used the wave function is given only by the contribution of the branch cut. For $|q| \leqslant 1/2$ it reads

$$\psi_{\mathrm{in}}(q,t) = \int_0^\infty \frac{\sqrt{\zeta} \cos(2\sqrt{\zeta}|q|) \exp[-i\zeta t]}{V_o^2[1 + \cos(2\sqrt{\zeta})]^2 + [\sqrt{\zeta} - V_o \sin(2\sqrt{\zeta})]^2}$$
$$\times \frac{d\zeta}{i\pi}, \tag{14}$$

while for $|q| > 1/2$,

$$\psi_{\mathrm{out}}(q,t) \tag{15}$$
$$= \int_0^\infty \frac{\cos(2\sqrt{\zeta}|q| + \theta(\zeta)) \exp[-i\zeta t]}{\sqrt{V_0^2[1 + \cos(2\sqrt{\zeta})]^2 + [\sqrt{\zeta} - V_o \sin(2\sqrt{\zeta})]^2}} \frac{d\zeta}{i\pi},$$

with the phase shift given by the expression

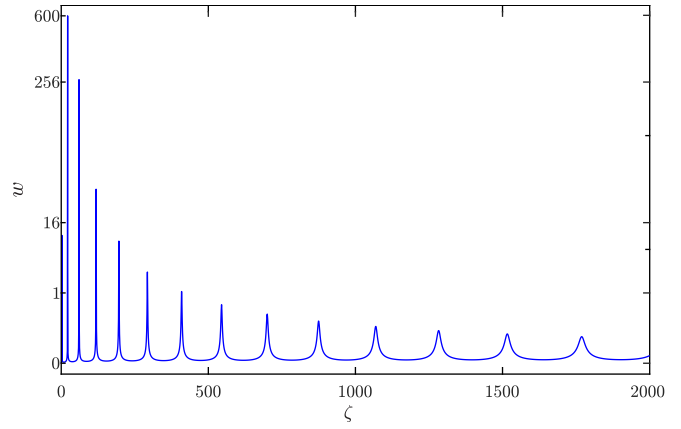$$\tan\theta(\zeta) = \frac{V_o[\cos(2\sqrt{\zeta}) + 1]}{\sqrt{\zeta} - V_o \sin(2\sqrt{\zeta})}. \tag{16}$$

FIG. 2. The weight function $w(\zeta)$ in the quartic-root scale for $V_o = 50$.

The derived solution is physically acceptable because it satisfies boundary conditions at the box walls,

$$\lim_{q \to \pm 1/2} \psi_{\mathrm{out}}(q,t) - \psi_{\mathrm{in}}(q,t) = 0,$$
$$\lim_{q \to \pm 1/2} \partial_q[\psi_{\mathrm{out}}(q,t) - \psi_{\mathrm{in}}(q,t)] \mp 4V_o\psi_{\mathrm{in}}(q,t) = 0, \tag{17}$$

and for $|q| \gg 1/2$ its probability current

$$j(q,t) \approx \frac{\mathrm{sgn}(q)}{2\pi^{3/2}\sqrt{t}} \tag{18}$$
$$\times \frac{|q|^2/t^2}{V_o^2\left[1 + \cos\left(2\frac{|q|}{t}\right)\right]^2 + \left[\frac{|q|}{t} - V_o \sin\left(2\frac{|q|}{t}\right)\right]^2}$$

is outward and finite [32]. For $V_o \to 0$ it becomes the inverse Laplace's transform of Eq. (5). When $V_o \to \infty$, the contribution of the branch cut (10) vanishes. Maxima $\lambda_n^{(\mu)}$ become poles at $\bar{\lambda}_n = -\epsilon_n$ associated with bound energies of the sealed box $\epsilon_n = (n + 1/2)^2\pi^2$, thus transforming Eq. (11) into

$$\psi(q,t) = -\sum_{n=1}^\infty 2\cos[(2n+1)\pi q]$$
$$\times \exp[-i(n+1/2)^2\pi^2 t]\Theta(1/2 - |q|), \tag{19}$$

a carpet formed only out of even states of the sealed box [8].

B. The resonant expansion

An approximate resonant expansion of ψ_{in} will be derived using an approach applicable also to ψ_{out}. Expression (14) represents a continuous superposition of waves $\cos(2\sqrt{\zeta}|q|) \exp[-i\zeta t]$ weighted by the function

$$w(\zeta) = \frac{1}{\frac{V_o^2}{\sqrt{\zeta}}[1 + \cos(2\sqrt{\zeta})]^2 + \sqrt{\zeta}\left[1 - \frac{V_o}{\sqrt{\zeta}}\sin(2\sqrt{\zeta})\right]^2}, \tag{20}$$

shown in Fig. 2. Its support is a set of narrow intervals whose width progressively becomes wider. Intervals are centered at minima ζ_n of the denominator function (20), where $w(\zeta)$ is equivalent to the Lorentzian of half width Γ_n, and amplitude Υ_n. Parameters of the Lorentzian assume particularly simple
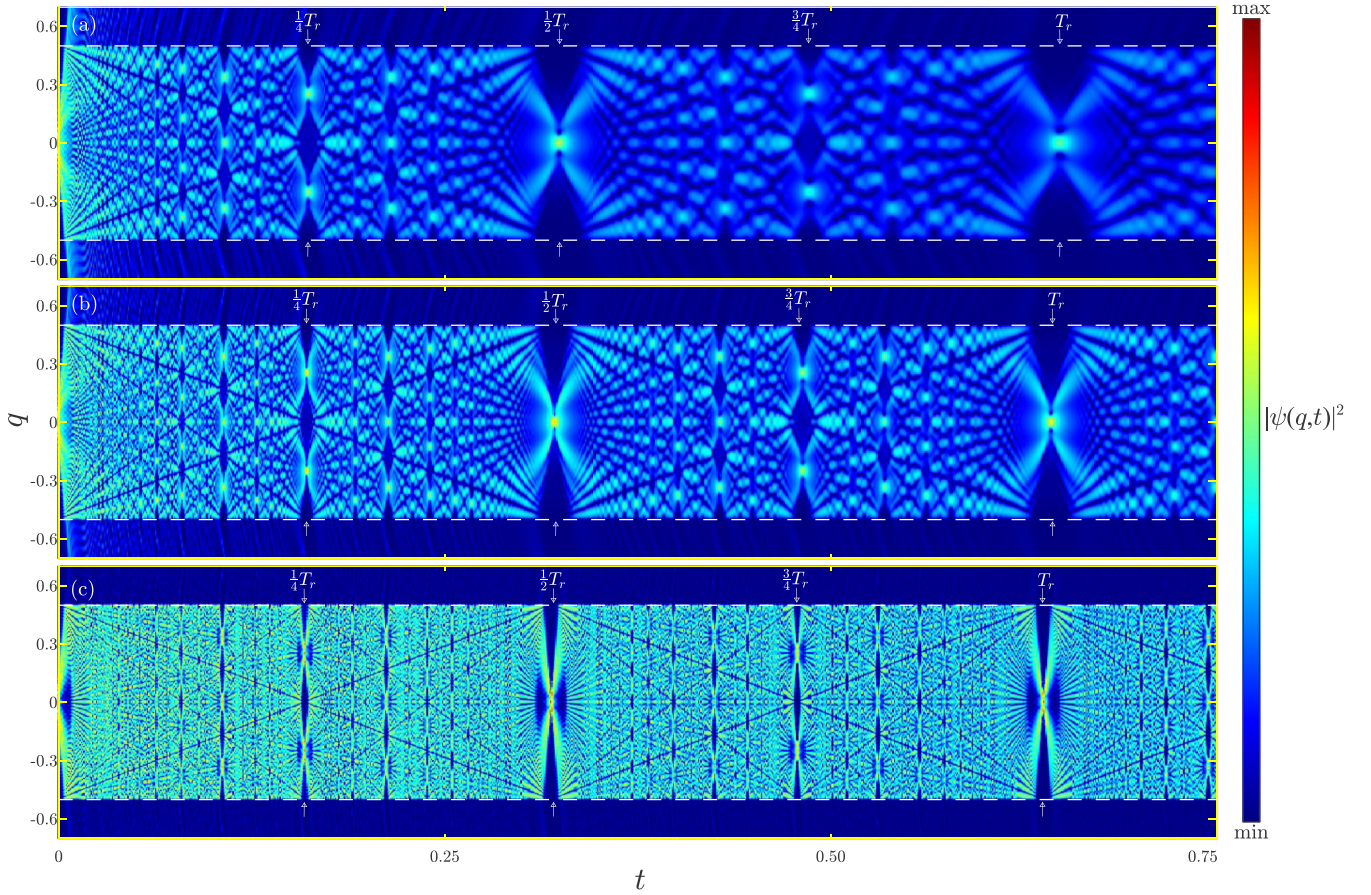
FIG. 3. The quantum carpet generated by the Ψ_1 for (a) $V_o = 50$, (b) $V_o = 100$, and (c) $V_o = 500$. The white dashed lines represent the walls of the box. Probability densities were color coded according to the shown color map. The arrows show time instances corresponding to $t = T_r/4, T_r/2, 3T_r/4,$ and T_r, respectively.

form for $v = 1/V_o$ small

$$
\zeta_n \approx \epsilon_n \left(1 - v + \frac{3v^2}{4}\right), \quad \Gamma_n \approx \frac{v^4 \epsilon_n^3}{2 + v^2 \epsilon_n}, \quad \Upsilon_n \approx \frac{4}{v^2 \epsilon_n^{3/2}}.
\tag{21}
$$

Consequently, ψ_{in} becomes

$$
\psi_{\text{in}}(q, t) \approx \sum_{n=1}^{N} \chi_n(q, t) + \chi_B(q, t),
\tag{22}
$$

where $\chi_n(q, t)$ is given by the integral

$$
\chi_n(q, t) \approx \int_0^\infty \Upsilon_n \Gamma_n^2 \frac{\cos(2\sqrt{\zeta}|q|) \exp[-i\zeta t]}{(\zeta - \zeta_n)^2 + \Gamma_n^2} d\zeta,
\tag{23}
$$

$\zeta_1 < \zeta_2 \cdots < \zeta_N$ is a set of maxima sufficiently distant and narrow to be considered as isolated, while $\chi_B(q, t)$ represents the correction of remaining maxima, that according to Eq. (14) and Fig. 2 is small.

Integrals (23) can be evaluated analytically [33], giving

$$
\chi_n(q, t) = \frac{\Upsilon_n \Gamma_n}{4i} \left[e^{i\bar{\phi}_n} E_1 \left(\frac{|q|^2}{it} + i\bar{\phi}_n \right) + e^{-i\phi_n} E_1 \left(\frac{|q|^2}{it} - i\phi_n \right) - e^{i\bar{\phi}_n^*} E_1 \left(\frac{|q|^2}{it} + i\bar{\phi}_n^* \right) - e^{-i\phi_n^*} E_1 \left(\frac{|q|^2}{it} - i\phi_n^* \right) \right],
\tag{24}
$$

where $\phi_n = \kappa_n |q| + \omega_n t$, $\bar{\phi}_n = \kappa_n |q| - \omega_n t$, $\kappa_n = 2\sqrt{\omega_n}$, $\omega_n = \zeta_n + i\Gamma_n$, and E_1 is the exponential integral [34]. Each term in Eq. (24) is finite because $e^z E_1(z) \to 1/z$ for z large. It can be understood as a renormalized Gamow state of energy ζ_n and half lifetime $1/\Gamma_n$ since the identical expression is valid for ψ_{out}.

C. Poincaré's recurrences

Figures 3(a)–3(c) show quantum carpets for $V_o = 50$, $V_o = 100$, and $V_o = 500$, respectively, calculated by a numerical

evaluation of integrals (14) and (15) using the z transformation [35]. The most prominent features of the observed carpets are full and fractional wave-packet revivals [9,10], and deep diagonal canals (also called intermode traces) that connect all regions, of very low density, located between reconstructed copies of the initial wave packet [8,36,37]. The time instances when the dynamics reconstruct the original wave packets and two of its copies are indicated by arrows. Figures 3(a)–3(c) show many other revivals occurring for $t = \frac{e}{f} T_r$ with e and f integers and mutually prime.
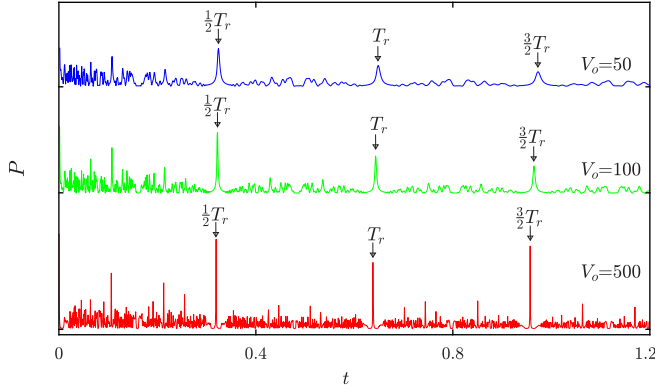
FIG. 4. The nondecay probabilities for $V_o = 50$, 100, and 500 in arbitrary units, shifted vertically for greater clarity.

According to theory, the evolution of the arbitrary initial state repeats after one revival time T_r, corresponding to the second full wave-packet revival [9,10]. For an even initial state of zero linear momentum, each full revival occurs at the initial position of the wave packet. This means that the period of such a carpet is $\frac{1}{2}T_r$. Thus, the revival times for carpets shown in Figs. 3(a)–3(c) are $T_r = 0.6481$, 0.6488, and 0.6378, respectively. Note that they are very close to the revival time of the carpet for the sealed box $T_o = 2/\pi = 0.6366$ [8].

To simplify the analysis of the wave-packet revivals we shall introduce a nondecay probability defined by the integral

$$P(t) = \left| \int_{-1/2}^{1/2} \psi_o^*(q)\psi_{\text{in}}(q,t)dq \right|^2 = |\psi_{\text{in}}(0,t)|^2, \quad (25)$$

that is, in this particular case, identical with the $q = 0$ slice through the carpet. The introduced quantity is much easier to calculate, and it is known to contain all essential information about the wave-packet revivals [9,10,38]. Figure 4 shows the obtained nondecay probabilities for $V_o = 50$, 100, and 500, respectively. Large peaks indicated by arrows correspond to full revivals occurring every $\frac{1}{2}T_r$. All other maxima occurring at $t = \frac{e}{f}T_r$ for odd f correspond to fractional revivals at the origin of the q axis. The lowest values (approximately zero, nondecay probability assumes for $t = \frac{e}{f}T_r$ and f even) correspond to wave-packet revivals occurring far from the origin of the q axis. It is interesting that the initial transient is observable of $t \leqslant \frac{1}{2}T_r$. For longer times, the established pattern repeats with a practically constant amplitude.

In the case of the sealed box, the scaling of the bound energies by a small factor $1 - v$, translates into the scaling of the carpet's period by $1 + v$ [10]. According to Eq. (21) the same scaling law should hold for the leaky box. Figures 3 and 4 prove that this is really the case. Numerically obtained ratios $T_r/T_o = 1.0018$, 1.0092, and 1.0181 for $V_o = 500$, 100, and 50 are in excellent agreement with the corresponding theoretical predictions $1 + 1/500 = 1.0020$, $1 + 1/100 = 1.0100$, and $1 + 1/50 = 1.0200$, respectively.

According to Eq. (21), as long as tunneling is low it cannot lead to detuning of resonant energies, and enables many repetitions of the observed stationary patterns shown in Figs. 3 and 4. This result shows that the validity of Poincaré's theorem can be extended to the case of the continuous spectrum,

with the small caveat that recurrences cannot occur infinitely often. The ratio $1/T_r\Gamma_1$ sets an upper bound to the number of Poincaré's recurrences that are in principle observable.

Figures 3 and 4 show that the quantum dynamics in a leaky box is unable to produce exact reconstructions of the initial wave packet. Its coherence loss will be examined in the following sections.

D. Decoherence of the quantum carpet

Using resonant expansion (22) the probability density of quantum carpet can be written in the following form,

$$|\psi_{\text{in}}(q,t)|^2 \approx \sum_{n=1}^{N} |\chi_n(q,t)|^2 + \sum_{n=1}^{N}\sum_{m>n}^{N}[\chi_n^*(q,t)\chi_m(q,t) + \chi_m^*(q,t)\chi_n(q,t)]. \quad (26)$$

The first term represents the probability density for the corresponding classical problem where the particle's state space consists of N distinct mutually exclusive states. The second term represents a distinctive modification of the classical theory, introduced by quantum formalism, that takes into account the interference between states. To judge the relative strength of the interference terms we shall use Eq. (24) to calculate a ratio,

$$r_{nm}(t) = \frac{\chi_n^*(q,t)\chi_m(q,t)}{|\chi_n(q,t)|^2}, \quad (27)$$

of nondiagonal and diagonal components of the density matrix for $t \to 0$,

$$r_{nm}(0) = \frac{\Upsilon_m\Gamma_m^2}{\Upsilon_n\Gamma_n^2} \lim_{t\to 0} \frac{\Gamma_n^2 t^4 + \left(t^2\zeta_n - \frac{1}{4}|q|^2\right)^2}{\Gamma_m^2 t^4 + \left(t^2\zeta_m - \frac{1}{4}|q|^2\right)^2} = \frac{\Upsilon_m\Gamma_m^2}{\Upsilon_n\Gamma_n^2}, \quad (28)$$

and $t \to \infty$,

$$r_{nm}(\infty) = \frac{\Upsilon_m\Gamma_m^2}{\Upsilon_n\Gamma_n^2} \lim_{t\to\infty} \frac{\Gamma_m^2 - 4\frac{|q|^4}{t^4} + \left(\zeta_m + \frac{|q|^2}{t^2}\right)^2}{\Gamma_n^2 - 4\frac{|q|^4}{t^4} + \left(\zeta_n + \frac{|q|^2}{t^2}\right)^2}$$
$$\times \left[\frac{\Gamma_n^2 + \left(\zeta_n - \frac{|q|^2}{t^2}\right)^2}{\Gamma_m^2 + \left(\zeta_m - \frac{|q|^2}{t^2}\right)^2}\right]^2 = \frac{\Upsilon_m\Gamma_m^2}{\Upsilon_n\Gamma_n^2}\frac{\zeta_n^2 + \Gamma_n^2}{\zeta_m^2 + \Gamma_m^2}. \quad (29)$$

For nondiagonal components, $m > n$. Consequently, $\zeta_m > \zeta_n$ and $\Gamma_m > \Gamma_n$. Equation (29) shows that interference terms are attenuated more than densities of individual resonances by a factor $(\zeta_m^2 + \Gamma_m^2)/(\zeta_n^2 + \Gamma_n^2)$ that is very large for $m \gg n$. Thus, the dynamics of the quantum carpet leads to decoherence, although tunneling alone is not capable of eradicating interference completely.

E. The coherence-loss analysis

The asymptotic analysis of the preceding section shows that decoherence manifests itself after a long time. However, Figs. 2 and 3 show that the deterioration of carpets occurs rather quickly. To get insight into how the carpet pattern forming ability is affected by tunneling we shall focus on the

$\psi_{\text{in}}(q = 0, t)$ slice for $V_o = 50$ and its Wigner-Ville transformation [39–41],

$$W(\omega, t) = \frac{1}{\pi} \int_{-\infty}^{\infty} \varphi^*(\omega + \eta) \varphi(\omega - \eta) \exp[2i\eta t] d\eta, \quad (30)$$

where $\varphi(\omega) = -i\sqrt{2} w(-\omega) \Theta(-\omega)/\pi$ is Fourier's transform of $\psi_{\text{in}}(0, t)$ transforming Eq. (30) into the form

$$W(\omega, t) = \frac{2}{\pi^2} \Theta(t) \Theta(-\omega)$$
$$\times \int_{-|\omega|}^{|\omega|} w(\omega + \eta) w(\omega - \eta) \exp[2i\eta t] d\eta. \quad (31)$$

Let us pick an arbitrary negative value $-\Omega$, and let $\zeta_1 < \cdots < \zeta_M$ be a list of all resonant energies not greater than 2Ω. For $-\Omega \leqslant \omega \leqslant 0$, and $t \geqslant 0$ the resonant expansion (22) can be used to approximate the Wigner-Ville transform by the following sums [42],

$$W(\omega, t) \approx \frac{1}{\pi^2} \left[\sum_n W_{nn}(\omega, t) + 2 \sum_n \sum_{m>n} W_{nm}(\omega, t) \right]. \quad (32)$$

Symbols W_{nm} denote a symmetrical matrix whose diagonal components are

$$W_{nn}(\omega, t) = \begin{cases} \pi(1 + 2\Gamma_n t) \exp[-2\Gamma_n t] \frac{\Upsilon_n^2}{\Gamma_n^3}, & \text{for } \omega = -\zeta_n, \\ \frac{2\pi}{|\omega_n|} \frac{\Upsilon_n}{\Gamma_n} \exp[-2\Gamma_n t] \cos(2\omega_n t), & \text{otherwise,} \end{cases} \quad (33)$$

where $\omega_n = |\omega| - \zeta_n$. Nondiagonal components are given by the expressions

$$W_{nm}(\omega, t) = 2\pi \rho_{nm} \exp[-2\Gamma_n t] \cos(2\omega_n t + \theta_{nm})$$
$$+ 2\pi \rho_{mn} \exp[-2\Gamma_m t] \cos(2\omega_m t + \theta_{mn}), \quad (34)$$

with

$$\rho_{nm} \exp[i\theta_{nm}] = \frac{a_{nm}}{\Gamma_n} + (\omega_n + i\Gamma_n) \frac{b_{nm}}{\Gamma_n}, \quad (35)$$

$$a_{nm} = \frac{8\bar{\xi}_{nm}^2 + 2\zeta_{nm}\bar{\xi}_{nm} + \Gamma_m^2 - \Gamma_n^2}{16\bar{\xi}_{nm}^4 + 8(\Gamma_n^2 + \Gamma_m^2)\bar{\xi}_{nm}^2 + \Gamma_m^2 - \Gamma_n^2} \Upsilon_n \Upsilon_m,$$

$$b_{nm} = \frac{4\bar{\xi}_{nm}}{16\bar{\xi}_{nm}^4 + 8(\Gamma_n^2 + \Gamma_m^2)\bar{\xi}_{nm}^2 + \Gamma_m^2 - \Gamma_n^2} \Upsilon_n \Upsilon_m, \quad (36)$$

while $\zeta_{nm} = \zeta_n - \zeta_m$, and $\bar{\xi}_{nm} = \bar{\xi}_{nm} - |\omega|$. Note that both $|W_{nn}|$ and $|W_{nm}|$ are very small unless $\omega \approx -\zeta_n$ and $\omega \approx -\bar{\xi}_{nm}$, respectively. At the resonant frequency, amplitudes ρ_{nm} have a maximum

$$\rho_{nm}(-\bar{\xi}_{nm}) = \frac{1}{\Gamma_n} \frac{\Upsilon_n \Upsilon_m}{\Gamma_m^2 - \Gamma_n^2}, \quad (37)$$

while the phases are $\theta_{nm}(-\bar{\xi}_{nm}) = 0$, transforming the matrix W_{nm} into

$$W_{nm}(-\bar{\xi}_{nm}) = \frac{4\pi \exp[-2\bar{\Gamma}_{nm}]}{\Gamma_m^2 - \Gamma_n^2} \sinh \left[\Gamma_{mn} t + \ln \sqrt{\frac{\Gamma_m}{\Gamma_n}} \right]$$
$$\times \frac{\Upsilon_n \Upsilon_m}{\sqrt{\Gamma_n \Gamma_m}} \cos(\zeta_{nm} t), \quad (38)$$

where $\bar{\Gamma}_{nm} = (\Gamma_m + \Gamma_m)/2$, and $\Gamma_{mn} = \Gamma_m - \Gamma_n$.

For any t the instantaneous spectrum of $\psi_{\text{in}}(0, t)$ consists of quasidiscrete resonant modes at $\omega = -\zeta_1, \ldots, -\zeta_M$ whose time development is given by Eq. (33). Figure 5(a). shows the first resonant mode at $\omega = -\zeta_1 = -2.419$ calculated by a numerical evaluation of Eq. (31) using the Chebyshev-Gaussian quadrature of high order [34]. The central ridge decay according to the first of Eq. (33) with a numerically obtained decay constant 0.0008 is very close to the theoretical value $\Gamma_1 = 0.001$. Parallel to the mode's backbone run is its associated add-modes whose evolution is given by the second of Eq. (33). The spectrogram also contains quasidiscrete shadow modes, generated by coupling between resonances, at $\omega = -\bar{\zeta}_{12}, \ldots, -\bar{\zeta}_{M-1,M}$. The evolution of its backbone is given by Eq. (38) while its add-modes evolve according to Eqs. (34)–(36). Figure 5(b) shows the first shadow mode at $\omega = -\bar{\zeta}_{12} = -12.095$, oscillating with a period 0.3247 which is extremely close to the theoretical prediction $2\pi/\zeta_{12} = 0.3250$.

Sometimes there will be l, n, and m such that $\zeta_l \approx \bar{\zeta}_{nm}$. In that case the spectrogram is given by the superposition $\frac{1}{\pi^2}[W_{ll}(\omega) + W_{nm}(\omega)]$. Such a mode will be considered as accidentally degenerate. An example of this behavior is shown in Fig. 5(c) showing a superposition of the resonant mode at $\omega = -\zeta_3 = -60.480$ and the shadow mode at $\omega = -\bar{\zeta}_{14} = -60.509$. Note that the shadow modes can also be accidentally degenerate. Higher-order degeneracies are possible, but in this particular study, they were not encountered.

According to the definition [41,43], the integral projection

$$\int_{-\infty}^{\infty} W(\omega, t) d\omega = |\psi(0, t)|^2 = P(t) \quad (39)$$

gives the blue nondecay probability curve from Fig. 4, while the integral projection

$$\int_{-\infty}^{\infty} W(\omega, t) dt = |\varphi(\omega)|^2 = \frac{2}{\pi^2} w^2(-\omega) \Theta(-\omega) \quad (40)$$

erases all traces of the shadow modes, leaving only resonant modes present in the power spectrum of the function $\psi_{\text{in}}(0, t)$. At the first glance, shadow modes seem to be physically unimportant mathematical artifacts that make interpretations of the spectrograms difficult. There are many proposals on how to eliminate them. Some authors use a Gaussian filter [44], while others combine it with the Gabor transformation [45]. On the contrary, it will be shown that shadow modes are very useful for the interpretation of structures generated by the wave packet's self-interference. Again, the analysis will be focused on the $q = 0$ slice of $\psi_{\text{in}}(q, t)$, but it can be applied, in the identical form, to any other slice.

In our subsequent analysis the following decomposition of the Wigner function,

$$W(\omega, t) = \mathfrak{W}(\omega, t) \cos[\mathfrak{w}(\omega, t)], \quad (41)$$

will be used. Function $\mathfrak{W}$ represents an amplitude of the phase-space probability density, while $\mathfrak{w}$ is the corresponding phase. Equations (33)–(38) show that if W is not negligible, its amplitude $\mathfrak{W}$ is an exponentially decreasing function of time. The phase $\mathfrak{w}$ is linearly proportional to time for shadow modes and exactly zero at the angular frequency of the resonant mode. It should be said that without an analytical solution such decomposition would be ambiguous since the second
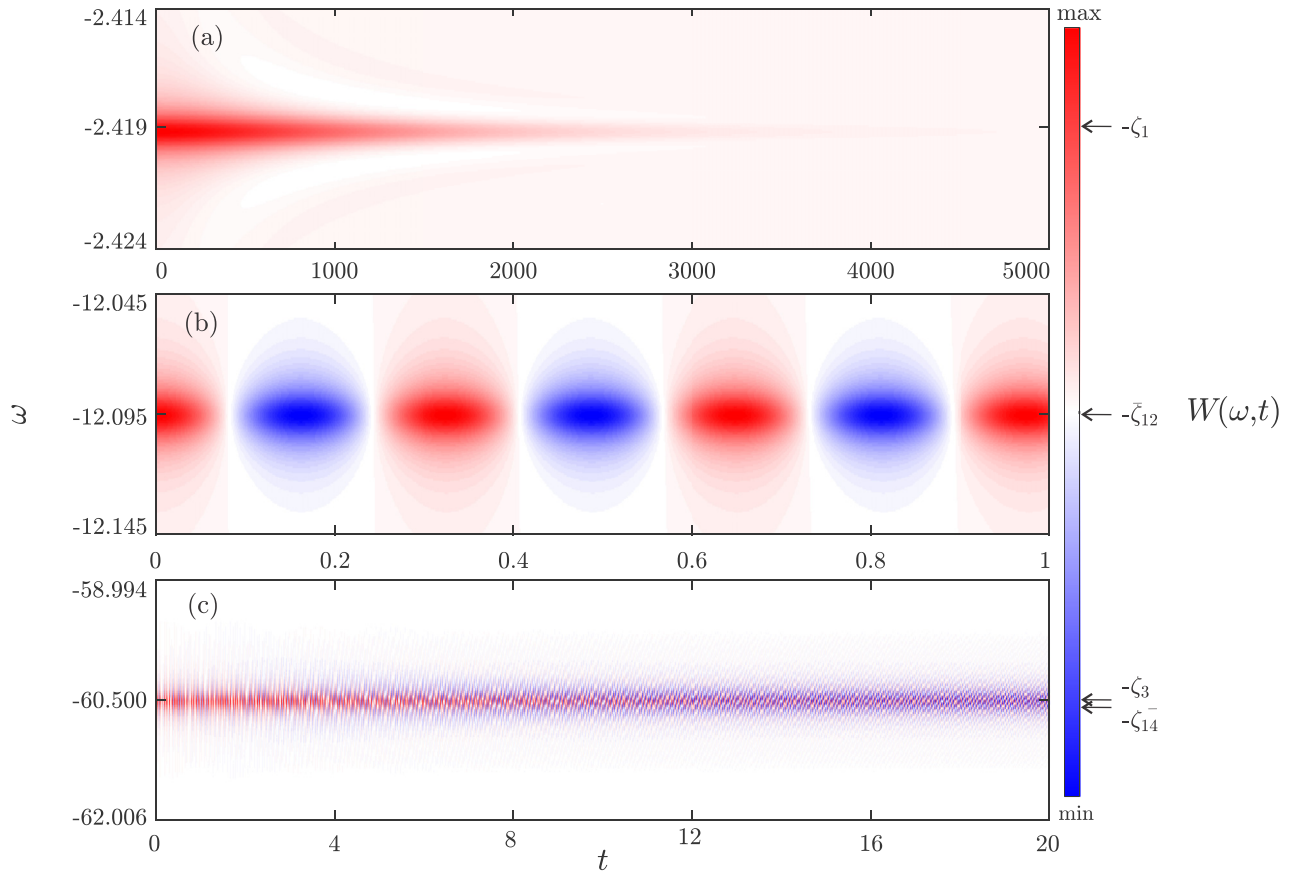
FIG. 5. The spectrograms of $\psi_{\text{in}}(0, t)$ for $V_0 = 50$ showing (a) resonant mode $\omega = -\zeta_1$, (b) shadow mode $\omega = -\bar{\xi}_{12}$, and (c) superposition of modes $\omega = -\zeta_3$ and $\omega = -\bar{\xi}_{14}$, respectively. Values of the Wigner function were color coded according to the shown color map.

independent equation, pinpointing the values of $\mathfrak{W}$ and $\mathfrak{w}$, is missing.

Figure 6(a) shows the obtained spectrogram for $0 \leqslant t \leqslant 0.02$ and $-350 \leqslant \omega \leqslant 0$ consisting of six resonant modes, each visible as a thin red line, and 24 shadow modes visible as a stripe of changing color. The complete list of modes in descending order can be found in Table I. Note that regions colored deepest red correspond to very large positive values of the Wigner function, i.e., $\mathfrak{w} \approx 2k\pi$ ($k \in \mathbb{N}$), while regions colored deepest blue correspond to very large negative values of the Wigner function, i.e., $\mathfrak{w} \approx (2k+1)\pi$. Between them are nodal regions where $W(\omega, t) \approx 0$, i.e., $\mathfrak{w} \approx (k + \frac{1}{2})\pi$ colored pale blue (almost white). The corresponding integral projection in the frequency direction containing singular peak at $t = 0$ is shown in Fig. 6(a′). This figure shows that the Dirac pulse is produced by a superposition of aligned maxima, elon-

gated along the t axis. The observed initial synchronization is a direct consequence of the fact that $\mathfrak{w}(\omega, 0) = 0$.

Figures 6(b) and 6(b′) show a spectrogram and its integral projection for a time interval centered at $\frac{1}{4}g_r T_r$. The irrational multiplier $g_r = \frac{1}{2}(\sqrt{5} - 1) = 0.618$ was chosen to avoid any fractional revivals. As it can be seen, the initial synchronization between maxima is lost, resulting in a very small value of the integral projection.

Figures 6(c) and 6(c′) show a spectrogram and its integral projection for a small time interval centered at $\frac{1}{4}T_r$. For $t = \frac{1}{4}T_r$ each maximum of the shadow mode can be paired with a minimum of the neighboring mode that results in their almost perfect cancellation by the integral projection. Thus, shadow modes can be divided into two groups perfectly synchronized among themselves, but with a phase shift of π between them. According to the theory [10] for $\frac{1}{4}T_r$ resonant states χ_n can

TABLE I. List of resonant modes in the descending order for $-350 \leqslant \omega \leqslant 0$. Pairs of bold symbols designate accidentally degenerate modes.

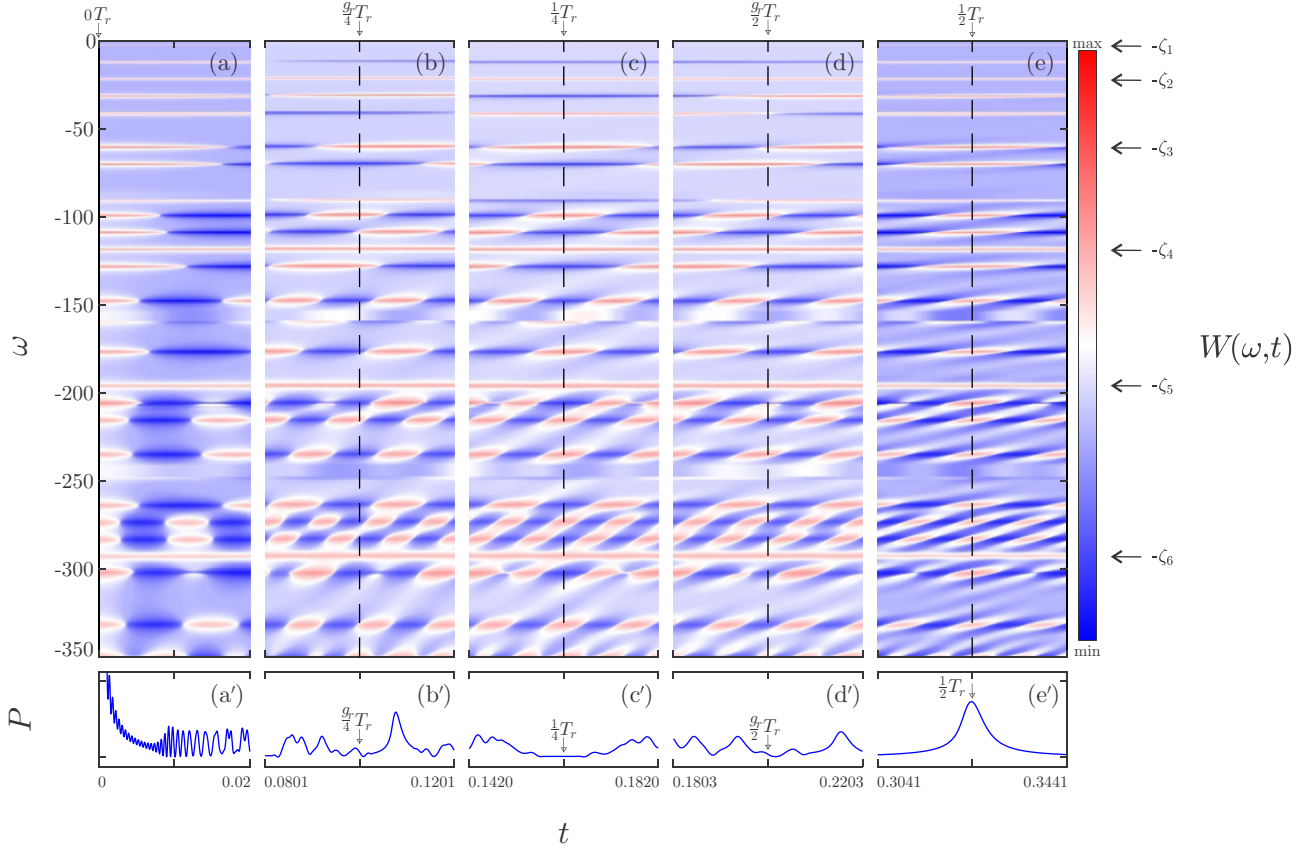| $-\zeta_1$	$-\bar{\xi}_{1,2}$	$-\zeta_2$	$-\bar{\xi}_{1,3}$	$-\bar{\xi}_{2,3}$	$-\boldsymbol{\zeta_3}$	$-\boldsymbol{\bar{\xi}_{1,4}}$	$-\bar{\xi}_{2,4}$	$-\bar{\xi}_{3,4}$	$-\bar{\xi}_{1,5}$
-2.419	-12.0945	-21.770	-31.449	-41.125	$\mathbf{-60.480}$	$\mathbf{-60.509}$	-70.185	-89.540	-99.209
$-\bar{\xi}_{2,5}$	$-\zeta_4$	$-\bar{\xi}_{3,5}$	$-\bar{\xi}_{1,6}$	$-\boldsymbol{\bar{\xi}_{4,5}}$	$-\boldsymbol{\bar{\xi}_{2,6}}$	$-\bar{\xi}_{3,6}$	$-\zeta_5$	$-\boldsymbol{\bar{\xi}_{4,6}}$	$-\boldsymbol{\bar{\xi}_{1,7}}$
-108.885	-118.600	-128.240	-147.659	$\mathbf{-157.300}$	$\mathbf{-157.335}$	-176.690	-196.000	$\mathbf{-205.750}$	$\mathbf{-205.809}$
$-\bar{\xi}_{2,7}$	$-\bar{\xi}_{3,7}$	$-\bar{\xi}_{5,6}$	$-\bar{\xi}_{4,7}$	$-\bar{\xi}_{1,8}$	$-\bar{\xi}_{2,8}$	$-\zeta_6$	$-\boldsymbol{\bar{\xi}_{5,7}}$	$-\boldsymbol{\bar{\xi}_{3,8}}$	$-\bar{\xi}_{4,8}$
-215.485	-234.840	-244.450	-263.900	-273.659	-283.335	-292.900	$\mathbf{-302.600}$	$\mathbf{-302.690}$	-331.750

FIG. 6. Spectrograms of $\psi_{\text{in}}(0, t)$ for $V_0 = 50$ in the vicinity of (a) $t = 0$, (b) $t = g_r T_r / 4$, (c) $t = T_r / 4$, (d) $g_r T_r / 2$, and (e) $T_r / 2$. (a′)–(e′) show corresponding integral projections of spectrograms in the frequency direction. Dashed black lines and arrows indicate the centers of the observed intervals. Black arrows indicate the positions of resonant modes. Values of Wigner functions were color coded according to the shown color map.

be grouped into two groups perfectly synchronized among themselves and mutually shifted by $\frac{\pi}{2}$ (which translates into a phase shift of π in the ω-t phase space) whose respective superposition reconstructs two copies of the initial wave packet at $q = \pm\frac{1}{4}$. As a consequence it produces a negligible probability density at $q = 0$ (see Fig. 3). Interestingly, even if we are analyzing only one slice of the quantum carpet its spectrogram contains essential information about the dynamics of the whole pattern.

Figure 6(d) and 6(d′) show a spectrogram and its integral projection for a small interval centered at $\frac{1}{2}g_r T_r$. The behavior of this spectrogram is identical to the one shown in Figs. 6(b) and 6(b′). The maxima and minima of spectral modes are again out of phase, resulting in a small value of the integral projection.

Figure 6(e) and 6(e′) show a spectrogram and its integral projection for a small interval centered at $\frac{1}{2}T_r$. For $t = \frac{1}{2}T_r$ there are no negative minima of the Wigner function, i.e., only its maxima are present. Their perfect alignment is responsible for the creation of a large maximum of nondecay probability by the integral projection that corresponds to the first full revival of the initial wave packet [see Fig. 3(a)].

At the first glance, it seems that different lifetimes of resonant states produce a distortion of the spectrum which only grows over time and acts as a low-pass filter, explaining why the initial wave packet cannot be reconstructed perfectly.

However, this explanation is not completely true. As it was shown in Sec. II D, noticeable effects of the finite lifetime appear only after a very long time. Thus, an explanation for nonperfect revivals should be looked for elsewhere.

A closer inspection of the spectrograms from Fig. 6 reveals that the dynamics changes the shape of the Wigner function extrema. Initially, all extrema are elongated along the t axis. Over time, elongation axes assume a positive angle with respect to the t axis, and the size of the extrema decreases. This effect is more pronounced when t or ω are large [see also Fig. 5(c)]. The reason for this behavior is that nodal lines of any shadow mode n, m are given by a family of hyperbolas $(2\omega + 2\bar{\zeta}_{nm} + \zeta_{nm})t = (k + \frac{1}{2})\pi$. Although the centers of extrema are aligned, the extrema of their add-modes are not, which inevitably introduces phase errors. Therefore, the described slight detuning of add-modes that produce the deformation of the shape of the Wigner function extrema is responsible for the imperfect reconstruction of the initial Dirac pulse.

III. CONCLUSIONS

It is shown that contrary to the firmly established belief, quantum carpets can be produced by the superposition of continuous states. This result suggests that it is possible to generalize the validity of Poincaré's recurrence theorem to

the continuous states, with the small caveat that reoccurrences cannot occur infinitely often. The model also provides additional insight into the carpet's coherence-loss process and can be used for a better understanding of quantum decoherence, which is extremely important in the current pursuit of a truly universal quantum computer. It has been shown that the ability of quantum interference to create sharp maxima is related to the shape of the Wigner function extrema, their orientation, and alignment. As a side result, the model provides a simple resonant expression of the wave function with resonances convergent in both space and time.

[1] M. Berry, I. Marzoli, and W. Schleich, Phys. World **14**, 39 (2001).

[2] K. Patorski, The self-imaging phenomenon and its applications, in *Progress in Optics*, edited by E. Wolf (North-Holland, Amsterdam, 1989), Vol. XXVII, pp. 1–108.

[3] M. V. Berry and S. Klein, J. Mod. Opt. **43**, 2139 (1996).

[4] M. J. Mark, E. Haller, J. G. Danzl, K. Lauber, M. Gustavsson, and H. Nögerl, New J. Phys. **13**, 085008 (2011).

[5] M. S. Chapman, C. R. Ekstrom, T. D. Hammond, J. Schmiedmayer, B. E. Tannian, S. Wehinger, and D. E. Pritchard, Phys. Rev. A **51**, R14 (1995).

[6] Z. Zhang, X. Liu, D. Zhang, J. Sheng, Y. Zhang, Y. Zhang, and M. Xiao, Phys. Rev. A **97**, 013603 (2018).

[7] L. B. Soldano and E. C. M. Pennings, J. Lightwave Technol. **13**, 615 (1995).

[8] M. V. Berry, J. Phys. A: Math. Gen. **29**, 6617 (1996).

[9] I. S. Averbukh and N. F. Perel'man, Zh. Eksp. Teor. Fiz. **96**, 818 (1989) [Sov. Phys. JETP **69**, 464 (1989)].

[10] R. Robinett, Phys. Rep. **392**, 1 (2004).

[11] D. Wallace, J. Math. Phys. **56**, 022105 (2015).

[12] G. Gamow, Z. Phys. **51**, 204 (1928).

[13] G. García-Calderón and R. Peierls, Nucl. Phys. A **265**, 443 (1976).

[14] A. Böhm and N. Harshman, Quantum theory in the rigged Hilbert space - Irreversibility from causality, in *Irreversibility and Causality, Semigroups and Rigged Hilbert Spaces*, Lecture Notes in Physics Vol. 504, edited by A. Bohm, H. Doebner, and P. Kielanowski (Springer, Berlin, 1996).

[15] J. Wen, Y. Zhang, and M. Xiao, Adv. Opt. Photonics **5**, 83 (2013).

[16] J. F. Clauser and J. P. Dowling, Phys. Rev. A **53**, 4587 (1996).

[17] K. Pelka, J. Graf, T. Mehringer, and J. von Zanthier, Opt. Express **26**, 15009 (2018).

[18] D. Bigourd, B. Chatel, W. P. Schleich, and B. Girard, Phys. Rev. Lett. **100**, 030202 (2008).

[19] O. J. Farias, F. de Melo, P. Milman, and S. P. Walborn, Phys. Rev. A **91**, 062328 (2015).

[20] P. T. Grochowski, T. Karpiuk, M. Brewczyk, and K. Rzazewski, Phys. Rev. Research **2**, 013119 (2020).

[21] M. Ćosić, S. Petrović, and S. Bellucci, Chaos **30**, 103107 (2020).

[22] M. Ćosić, S. Petrović, and S. Bellucci, Sci. Rep. **10**, 16949 (2020).

[23] M. Ćosić, S. Petrović, and Y. Takabayashi, Phys. Rev. A **103**, 022818 (2021).

[24] P. Kazemi, S. Chaturvedi, I. Marzoli, R. F. O'Connell, and W. P. Schleich, New J. Phys. **15**, 013052 (2013).

[25] E. Honrubia and A. S. Sanz, Phys. Rev. A **103**, 062210 (2021).

[26] R. Bonifacio, I. Marzoli, and W. P. Schleich, J. Mod. Opt. **47**, 2891 (2000).

[27] Y. Elran and P. Brumer, J. Chem. Phys. **121**, 2673 (2004).

[28] Y. Elran and P. Brumer, J. Chem. Phys. **138**, 234308 (2013).

[29] A. S. Sanz, Can. J. Chem. **92**, 168 (2014).

[30] C. Grosche, Ann. Phys. **505**, 557 (1993).

[31] The derivation uses identity (7.4.3) of Ref. [34].

[32] The derivation uses the stationary phase approximation.

[33] The derivation uses identity (7.4.10) of Ref. [34].

[34] M. Abramowitz and I. Stegun, *Handbook of Mathematical Functions* (National Bureau of Standards, Washington, DC, 1972).

[35] *Theory and Application of Digital Signal Processing*, edited by L. R. Rabiner and B. Gold (Prentice Hall, New Jersey, 1975).

[36] A. E. Kaplan, I. Marzoli, W. E. Lamb, and W. P. Schleich, Phys. Rev. A **61**, 032101 (2000).

[37] A. E. Kaplan, P. Stifter, K. A. H. van Leeuwen, W. E. Lamb, and W. P. Schleich, Phys. Scr. **T76**, 93 (1998).

[38] G. Casati, G. Maspero, and D. L. Shepelyansky, Phys. Rev. Lett. **82**, 524 (1999).

[39] T. A. C. M. Claasen and W. F. G. Mecklenbrauker, Philips J. Res. **35**, 217 (1980).

[40] E. Wigner, Phys. Rev. **40**, 749 (1932).

[41] R. Kubo, J. Phys. Soc. Jpn. **19**, 2127 (1964).

[42] The derivation uses identity (4.3.146) of Ref. [34].

[43] V. I. Tatarskii, Sov. Phys. Usp. **26**, 311 (1983).

[44] K. Husimi, Proc. Phys.-Math. Soc. Jpn. **22**, 264 (1940).

[45] S. C. Pei and J. J. Ding, IEEE Trans. Signal Process. **55**, 4839 (2007).